

Article

Ultrasound Assisted Casting of an AM60 Based Metal Matrix Nanocomposite, Its Properties, and Recyclability

Hajo Dieringa ^{1,*} , Lydia Katsarou ¹, Ricardo Buzolin ¹, Gábor Szakács ¹, Manfred Horstmann ¹, Martin Wolff ¹, Chamini Mendis ^{1,2}, Sergey Vorozhtsov ³ and David StJohn ⁴ 

¹ Institute of Materials Research, Helmholtz-Zentrum Geesthacht, Max-Planck-Str. 1, 21502 Geesthacht, Germany; lydiapvnrt@gmail.com (L.K.); ricardo.buzolin@tugraz.at (R.B.); gabor.szakacs@hzg.de (G.S.); manfred.horstmann@hzg.de (M.H.); martin.wolff@hzg.de (M.W.); chamini.mendis@brunel.ac.uk (C.M.)

² BCAST-Brunel Centre for Advanced Solidification Technology, Brunel University, Uxbridge, Middlesex UB8 3PH, UK

³ Faculty of Physics and Engineering, National Research Tomsk State University, Tomsk 634050, Russia; vorn1985@gmail.com

⁴ Centre for Advanced Materials Processing and Manufacturing, School of Mechanical and Mining Engineering, The University of Queensland, Brisbane, QLD 4072, Australia; d.stjohn@uq.edu.au

* Correspondence: hajo.dieringa@hzg.de; Tel.: +49-4152-871955

Received: 16 August 2017; Accepted: 19 September 2017; Published: 22 September 2017

Abstract: An AM60 magnesium alloy nanocomposite reinforced with 1 wt % of AlN nanoparticles was prepared using an ultrasound (US) assisted permanent-mould indirect-chill casting process. Ultrasonically generated cavitation and acoustic streaming promoted de-agglomeration of particle clusters and distributed the particles throughout the melt. Significant grain refinement due to nucleation on the AlN nanoparticles was accompanied by an exceptional improvement in properties: yield strength increased by 103%, ultimate tensile strength by 115%, and ductility by 140%. Although good grain refinement was observed, the large nucleation undercooling of 14 K limits further refinement because nucleation is prevented by the formation of a nucleation-free zone around each grain. To assess the industrial applicability and recyclability of the nanocomposite material in various casting processes, tests were performed to determine the effect of remelting on the microstructure. With each remelting, a small percentage of effective AlN nanoparticles was lost, and some grain growth was observed. However, even after the third remelting, excellent strength and ductility was retained. According to strengthening models, enhanced yield strength is mainly attributed to Hall-Petch strengthening caused by the refined grain size. A small additional contribution to strengthening is attributed to Orowan strengthening.

Keywords: nanoparticles; metal matrix nanocomposite (MMNC); AlN; magnesium alloy AM60; strengthening mechanisms

1. Introduction

Magnesium alloys have been in use for over 90 years in weight critical applications. During the last few decades, disadvantages such as vulnerability to corrosion, limited high temperature strength, and creep resistance have been overcome by the development of advanced magnesium alloys containing rare earth elements [1–3], calcium [4,5], strontium [6,7], tin [8,9], or barium [10]. However, improvements achieved through novel alloy development are limited. This limit can only be overcome through reinforcing magnesium alloys with particles or fibres, similar to metal matrix composites (MMCs). Use of microscale reinforcements significantly improves the strength [11,12], wear [13],

creep resistance [14–16], and fatigue strength [17,18]. However, these improvements require the addition of 10–40% of reinforcement. This high amount usually increases the density of the material significantly and lowers the ductility making it unsuitable for light weight applications.

The addition of 0.5 wt % AlN particles of less than 5 μm size to a Mg-3Al alloy reduced the grain size to 120 μm from 450 μm without AlN addition [19]. Defining a grain size reduction (GSR) by [20] $\text{GSR} = \left(\frac{1}{\sqrt{D_{\text{MMNC}}}} - \frac{1}{\sqrt{D_0}} \right)$, a value of $4.41 \times 10^{-2} \mu\text{m}^{-1/2}$ has been achieved. The premise for comparing GSR values is that the casting parameters are similar and there are no other influences that may affect grain size.

For several years now, nano sized particles have been used as reinforcement for metal matrix nanocomposites (MMNCs), and the number of publications on MMNC research is increasing, see Figure 1. The main reason for this increase is the dramatic reduction in the price of nanoparticles. Particles with a diameter below 100 nm have an ideal size for Orowan strengthening, even if only small amounts are added when uniformly distributed in the matrix. Paramsothy and Gupta published a study on the addition of 1.5 vol % AlN particles of 10 nm–20 nm in size to an AZ91/ZK60 hybrid alloy [21,22]. This material was processed by Disintegrated Melt Deposition (DMD) followed by hot extrusion. Although they did not observe any effect on grain size, the ductility slightly decreased, and tensile yield strength slightly increased. An overview of nanoparticle reinforced magnesium alloys is given in [23].

It is difficult to uniformly distribute nanoparticles in metallic melts because of their high surface area and the poor wettability of nanoparticles by the metallic melt. A uniform distribution can be easily produced with powder metallurgical processes but these processes are costly and cannot easily be used for mass production. Other melt metallurgical processes such as DMD [24,25] or an evaporation of magnesium after casting [26] have a scientific focus, but are not commercially viable. Conventional casting processes which require only slight modifications for distributing nanoparticles, are, therefore, a field of interest for research as well as for industry. For this reason, the European Project ExoMet was established to explore novel grain refining and nanoparticle additions in conjunction with melt treatment by means of external fields (electromagnetic, ultrasonic, and mechanical). These external fields provide an effective and efficient method to disperse the nanoparticles into the melt with uniform distribution in the as-cast material [27]. Of these fields, ultrasonic treatment is ideal as the ultrasound waves and cavitation under the ultrasound probe promote de-agglomeration of particle clusters and particle wetting. Also, acoustic streaming facilitates vigorous convection transporting the released particles throughout the melt. Magnesium alloy Elektron21 has been successfully reinforced with 1 wt % AlN nanoparticles and it was shown that AlN-reinforced Elektron21 has significantly improved creep resistance at 240 °C [28]. At low stresses, the minimum creep rate is nearly one order of magnitude lower compared to that of the unreinforced Elektron21, although Elektron21 is already one of the most creep resistant commercially available magnesium alloys. SEM and TEM investigations showed that the AlN nanoparticles are located in the eutectic region and in primary magnesium grains close to the eutectic region. The nanoparticles seem to strengthen the eutectic region, which ultimately results in creep strengthening of the nanocomposite. The reason for this may be that the particles tend to prevent the material from grain boundary sliding by strengthening the eutectic and grain boundary regions [28].

In this paper, we investigate microstructural features, strength, and recyclability of conventional magnesium High Pressure Die Casting (HPDC) alloy AM60 reinforced with 1 wt % of AlN nanoparticles and compare it to those of unreinforced AM60 processed using ultrasound assisted casting in both cases.

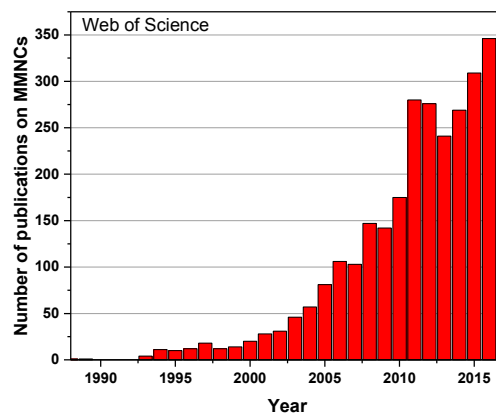


Figure 1. Number of publications on metal matrix nanocomposites (MMNCs) in Web of Science.

2. Materials and Methods

A commercial magnesium alloy AM60 was selected as it is widely used in the manufacture of high pressure die castings for the automotive industry. The nominal composition according to the supplier, MAGONTEC, of AM60 alloy is Mg-6Al-0.4Mn (wt %). The AlN nanoparticles were processed at Tomsk State University, in Russia, using electric explosion of aluminium metal wire in a nitrogen-containing atmosphere [29]. The medium particle size is 80 nm. Figure 2a shows typical particles and Figure 2b shows the particle size distribution.

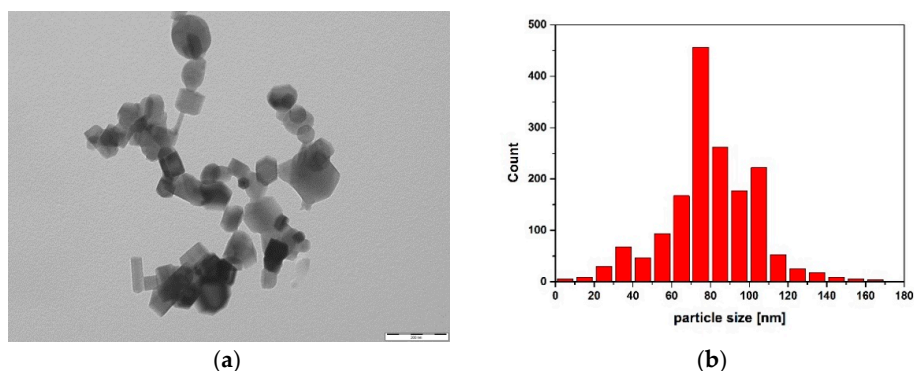


Figure 2. (a) Typical AlN nanoparticles (scale bar: 200 nm) and (b) their particle size distribution.

Approximately 3 kg of molten AM60 alloy at 720 °C was poured into a preheated cylindrical mould (450 °C), which was then placed within a three-zone resistance ring furnace (ThermConcept, Bremen, Germany) for maintaining the temperature of the melt at 670 °C. After creating a vortex by mechanical stirring (200 rpm), AlN nanoparticles wrapped in aluminium foil were introduced to the melt. As soon as the particles were no longer on the top of the melt, ultrasonic (0.3 kW, 20 kHz) stirring was applied for 5 min to disperse the particle clusters. After mixing, the stirrer and the ultrasound probe were removed from the melt and the mould was lowered mechanically into a water bath directly underneath the furnace opening. A steel mould (St52 or 1.0831) with 3 mm wall thickness was used. As the mould was lowered into the water bath at a speed of 3 mm/s, solidification initiated at the bottom and preceded upwards allowing shrinkage to be fed by the remaining melt above the solid-liquid interface producing very dense castings. This process was invented in the 1930s by the I.G. Farbenindustrie AG in Germany for production of slabs for rolling or extrusion. The cover gas, 1 vol % SF₆ with Ar, was used during the whole casting process at a constant flux.

For comparison, AM60 without nanoparticles was cast in the same way including mechanical and US assisted stirring. Cylinders of 100 mm diameter and a length of 250 mm were cast, and slices

of 10 mm thickness were cut from the middle of the casting at a height of 125 mm. After extracting this slice for metallography and tensile test specimens, the remaining parts were remelted at a temperature of 670 °C in the mould. The melt was only slightly mechanically stirred and after holding for 5 min, the melt solidified as described above to obtain the first recycled cylinder from which a slice was cut out from the same area as was done in the first experiment. This process was repeated two more times in order to obtain three recycled and remelted cylinders from which the role of AlN nanoparticles during recycling could be elucidated.

Spiral casting experiments were performed with a spiral mould preheated to 375 °C and both melts of AM60 and AM60 containing AlN nanoparticles had a melt temperature of 675 °C. The length of the cast spiral was taken as a measure of relative viscosity of the melt. DSC (Differential Scanning Calorimetry) measurement was done with a DSC 2 from Mettler Toledo (Mettler-Toledo, Greifensee, Switzerland). Three heating and cooling cycles between 400 °C and 700 °C, from which the last two cycles were used for determination of the undercooling at the start of solidification. Density was determined following the Archimedean Principle by measuring the weight five times in air and ethanol with a Sartorius balance LA230S (Sartorius, Göttingen, Germany).

To study the microstructure, samples were cut from the slice at approximately 10 mm from the surface and were cold mounted using epoxy resin. Samples were ground (800, 1200, and 2500 grit) and hardness values were measured with an EMCO M1C 010 testing machine (EMCO-TEST, Kuchl, Austria) using a 5 kg load. The samples were ground with 2500 grit after the hardness tests and polished with a 1 µm diamond solution in OPS (oxide polishing suspension). The surface of the sample was etched with a 9 vol % picric acid solution and optical micrographs were recorded using polarised light microscopy with Nomarski contrast to see the grain structures.

Five micro-tensile specimens (gauge length: 9 mm, cross section 2 mm × 2 mm) were electro-discharge machined from the slices of the castings. The room temperature tensile tests were conducted using a 5 kN universal tensile testing machine (Zwick-Roell, Ulm, Germany) and the displacement was measured with a laser extensometer (Fiedler Optoelektronik GmbH, Lützen, Germany).

Scanning electron microscopy was performed using a Tescan Vega3 SEM (TESCAN ORSAY, Brno, Czech Republic) equipped with Tescan Energy dispersive X-ray (EDX) spectrometer. EDX spectra maps were measured in order to identify possible sites with a higher concentration of nitrogen. For calculations of the mismatch between AlN and Mg the crystal structures of Mg were generated with CaRIne crystallographic software TM (CaRIne 3.1, Software CaRIne Crystallography, Senlis, France, 2015) using data available in Pearsons crystallographic databases [30].

3. Results

3.1. Microstructure

The castings have a very uniform microstructure with less than 1% porosity and appear free of segregation. The optical micrographs in Figure 3 show that the addition of AlN refined the grain size significantly and the morphology of the grains changed from dendritic to a more equiaxed structure, Figure 3a,b. The measured grain size shows a significant reduction from $1277.0 \pm 301.3 \mu\text{m}$ to $84.9 \pm 6.2 \mu\text{m}$ due to the addition of nanoparticles to the AM60 alloy produced in a similar manner. Figure 3c–e and Table 1 show the microstructures and properties following recycling through remelting, with each remelting step increasing the grain size to $196.4 \pm 16.0 \mu\text{m}$ after the third remelting cycle. Grain size distribution graphs of all AlN containing materials are shown in Figure 3f–i. The measured density and amount of porosity in the castings are given in Table 1. The amount of porosity was calculated assuming a theoretical density of 1.799552 g/cm^3 for AM60 + 1 wt % AlN and the results do not differ significantly.

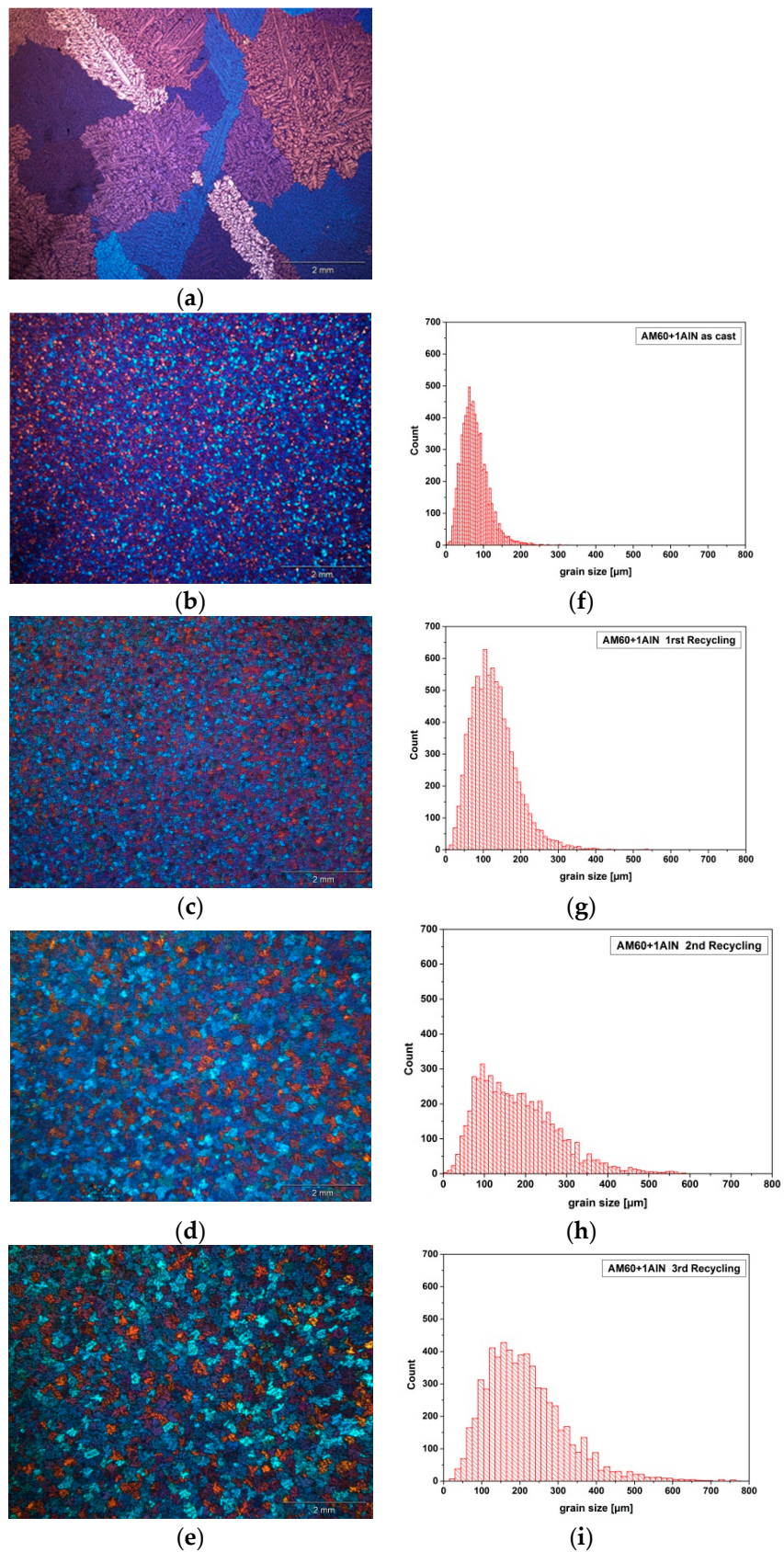


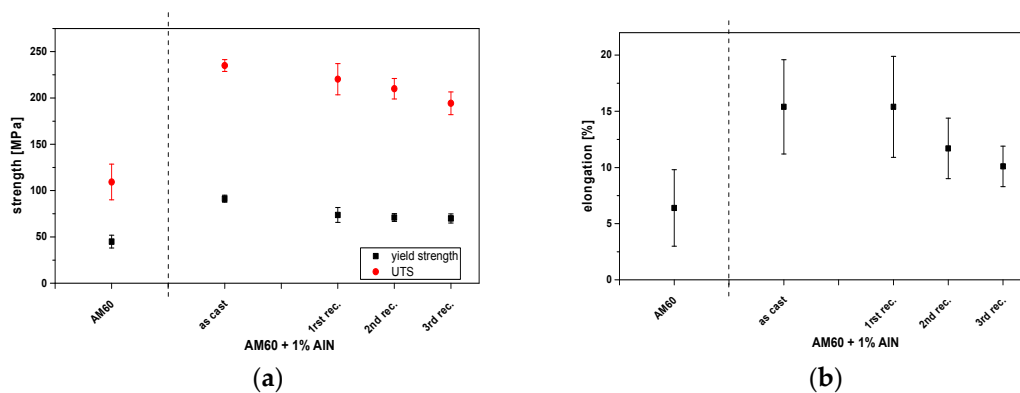
Figure 3. Microstructures of (a) AM60 and (b) AM60 + AlN. Microstructures of the first, second, and third recycled castings are shown in (c–e), respectively. Grain size distributions of (b–e) are presented in (f–i), respectively.

Table 1. Grain size, hardness, density, percent porosity, and the mechanical properties of the investigated materials. UTS = ultimate tensile strength.

Property	AM60	AM60 + AlN	1st Recycling	2nd Recycling	3rd Recycling
Grain size (μm)	1277.0 \pm 301.3	84.9 \pm 6.2	113.8 \pm 22.1	176.8 \pm 12.9	196.4 \pm 16.0
Hardness (HV5)	48.0 \pm 4.0	46.4 \pm 6.0	50.9 \pm 1.1	47.8 \pm 1.0	48.5 \pm 2.6
Density (g/cm^3)	1.7848 \pm 0.0004	1.783 \pm 0	1.7842 \pm 0.00075	1.7852 \pm 0.0004	1.785 \pm 0
Porosity (%)	-	0.919	0.853	0.797	0.808
Yield strength (MPa)	44.9 \pm 6.9	91.2 \pm 3.8 $\Delta = 46.3$	73.7 \pm 8.1 $\Delta = 28.8$	70.9 \pm 4.3 $\Delta = 26.0$	69.9 \pm 5.0 $\Delta = 25.0$
UTS (MPa)	109.3 \pm 19.2	235.1 \pm 6.4	220.3 \pm 16.8	210.0 \pm 11.0	194.3 \pm 12.3
Elongation (%)	6.4 \pm 3.4	15.4 \pm 4.2	15.4 \pm 4.5	11.7 \pm 2.7	10.1 \pm 1.8

3.2. Mechanical Properties

The room temperature tensile tests show a remarkable increase in the yield strength (YS) and the ultimate tensile strength (UTS) after ultrasound (US) assisted addition of 1 wt % AlN nanoparticles, with both values being over twice that of the alloy without AlN nanoparticles, Table 1 and Figure 4a. There is an increase of 103% in YS and 115% in UTS. An increase of 140% was observed in the elongation to failure with the addition of AlN nanoparticles, Figure 4b. As mentioned, the reinforcement of micro-particles or fibres usually lowers the ductility significantly, but in this case, the AlN nanoparticle addition more than doubles the elongation to failure. Grain refinement often has a positive effect on ductility [31–33], although there is not a direct relationship between the two as other factors such as casting defects and the presence of intermetallic phases can also affect ductility. In this work, the absence of macroscopic cracking at twin boundaries is assumed to be the reason for improved ductility [33].

**Figure 4.** Mechanical properties: (a) yield and ultimate tensile strength and (b) elongation to fracture.

4. Discussion

AlN has a hexagonal crystal structure with the lattice parameters $a = 0.311$ nm and $c = 0.498$ nm, and Mg has the same lattice structure with lattice parameters of $a = 0.321$ nm and $c = 0.512$ nm [30]. The mismatch between Mg and AlN was approximately 3.1% between the $\{10\bar{1}0\}$ planes and 2.7% along the (0001) planes. The close matching between Mg and AlN is illustrated in Figure 5. Similar mismatches were observed on other major planes of AlN and Mg. The similarities in crystal structure and lattice parameter means that growth of Mg on an AlN particle is relatively easy and does not require accommodation of large strain, and the differences in lattice parameter can be overcome locally in the first layers of Mg that grow on the AlN particles.

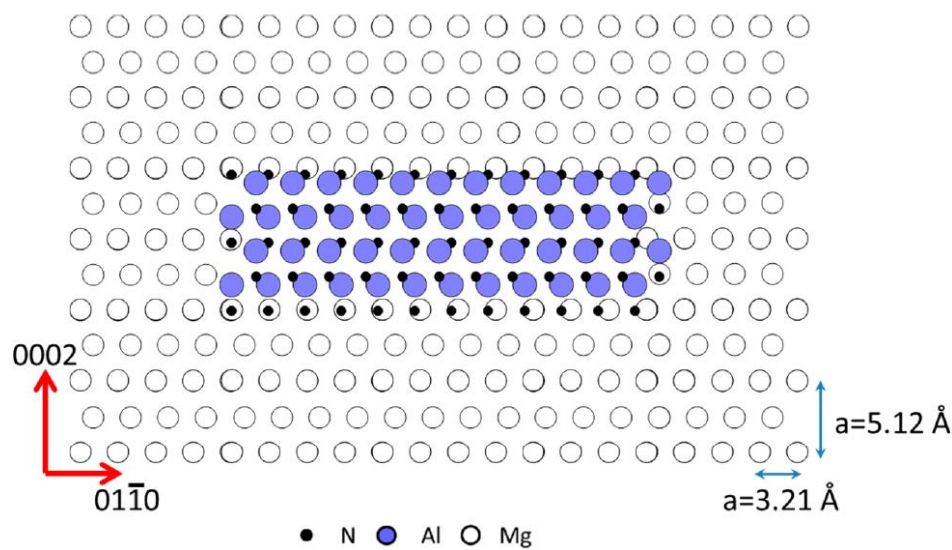


Figure 5. Crystallography of an AlN particle within a magnesium matrix.

4.1. Microstructure

The grain size can be assumed to be the average distance between successful nucleation events [34]. The number of particles added per gram of AlN powder of 80 nm average size is estimated to be 1.15×10^{15} . The largest particles were measured to be 162 nm and represent 0.003% of the total number of particles. The number of particles per gram was converted to the number of particles per volume. Assuming complete mixing of particles occurs during US, the average spacing between the largest particles would be 2.1 μm . If we also assume that the largest particles have the highest nucleation potencies [34,35] and that all of these nucleate a grain, then the grain size would be 2.1 μm compared with a measured average grain size of 84.9 μm . This indicates that only a very small fraction (approximately 0.002%) of the largest 0.003% of particles successfully nucleate a grain.

Several factors could reduce the number of nucleation events. One is particle agglomeration. Another is fading due to density differences where the higher density AlN particles sink to the bottom of the casting. These two factors are probably playing a role in the increased grain size obtained after each reheating cycle. Another cause may be particle pushing in front of a growing grain, although one might expect this to decrease the grain size. However, no localised increase in nitrogen content was observed at grain boundaries, suggesting particle pushing does not occur to a significant degree during solidification.

Considering the particle size distribution, it may be that only the very largest particles within the 162 nm band are effective nucleants. However, the alloy chemistry may have a more significant effect on grain size because of the formation of a large nucleation-free zone (NFZ) which prevents nucleation in a region around each newly formed grain. In other research [36] it was found that NFZ was the dominant factor setting the grain size of Mg-Al alloys. In fact, the final as-cast grain size was approximately equal to that in the NFZ. It was proposed that a very high density of nucleant particles naturally exist in the melt, such that a particle of suitably high potency is present at the end of NFZ where $\Delta T_{CS} = \Delta T_n$ triggers nucleation. The size of NFZ is calculated by the equation:

$$\text{NFZ} = \frac{D \cdot z \Delta T_n}{v \cdot Q} + \frac{4.6D}{v} \left(\frac{C_1^* - C_0}{C_1^* \cdot (1 - k)} \right) \quad (1)$$

where D is the diffusion coefficient of solute in the liquid, v the velocity of the growing solid-liquid interface, Q the growth restriction factor, C_1^* the composition of the liquid at the solid-liquid interface, C_0 the composition of the alloy, ΔT_n the nucleation undercooling, k the partition coefficient, and z the

fraction of ΔT_n required to trigger the next nucleation event. The first term is the amount of growth required to create enough constitutional supercooling, ΔT_{CS} , to equal the nucleation undercooling of the nucleant particle, ΔT_n . The second term is the length of the constitutionally supercooled region in front of the growing grain's interface to the end of the diffusion field where $\Delta T_{CS} = \Delta T_n$. Given the number of particles of 162 nm (3.45×10^{12}), it can be assumed that there are sufficient particles to nucleate a grain as soon as $\Delta T_{CS} = \Delta T_n$ is reached (i.e., grain size equals NFZ).

ΔT_n was determined from DSC to be 14 K (16 K for AM60 without AlN present). Despite the good orientation relationship between AlN and α -Mg (above), the measured undercooling is in keeping with the Free Growth Model [35], which predicts a large nucleation undercooling due to the nanoscale size of the AlN particles. Using Equation (1) with Q of 26 K for AM60, D of 5×10^{-9} m²/s and v of 5×10^{-6} μ m/s, NFZ is of the order of 600 μ m. D and v are estimates based on literature data [36]. The growth velocity v will initially be faster at an undercooling of 14 K (i.e., higher driving force) than for more potent particles. However, to reduce NFZ from 600 to about 85 μ m, v would need to be about seven times faster. No data exist to verify a change of this magnitude, but given the casting rate of 3 mm/s, v may be considerably faster. On the other hand, because the grain size is relatively small, solute accumulation between the grains early in solidification will reduce the amount of constitutional supercooling which can quickly reduce v [34]. Reducing D to 7×10^{-10} m²/s results in an NFZ (i.e., assumed to equal the grain size) of 89 μ m. A possible reason for a lower diffusion coefficient is the impediment to diffusion caused by the very high density of particles (increased viscosity suggests a slower diffusion rate [37]). This effect was observed in the spiral casting tests where the length of the spiral was 96.2 cm for AM60 and 83.5 cm for AM60 + AlN. Therefore, it is possible that hypothesized changes to both v and D contribute to a reduction in the size of NFZ. Thus, the formation of NFZ during solidification prevents nucleation on many of the suitably potent particles present in the melt, reducing the potential for achieving a very fine grain size, for example, of less than 20 μ m.

4.2. Mechanical Properties

A Hall-Petch diagram including the remelted nanocomposites is shown in Figure 6. It presents the relationship between the yield strength and the reciprocal of the square root of grain size (D) for AM60 and the AM60 based nanocomposites. According to the Hall-Petch relation (Equation (A1) in Appendix A) σ_0 was found to be 30.2 MPa and k_y to be 530.2 MPa μ m^{1/2}.

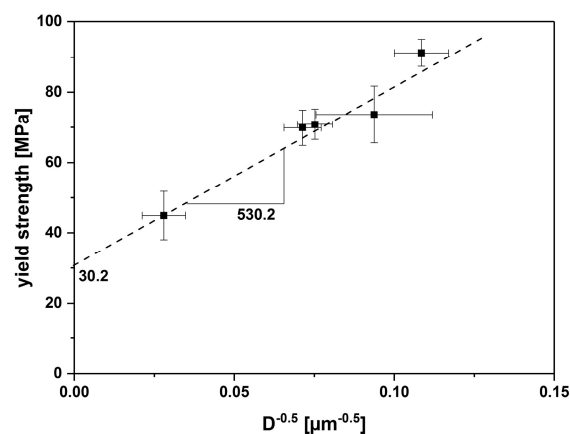


Figure 6. Hall-Petch plot of yield strength over the reciprocal of the square root of grain size D following Equation (A1) in Appendix A. (The standard deviation of the square root D is given in percentage of standard deviation of D and a minimum square root fit was applied without considering the standard deviations).

We have shown that the mechanical properties are comparable to HPDC, but without HPDC's inherent porosity (which can be up to 5%). Thus, the nanocomposites would be heat treatable

and weldable, which is not possible with HPDC castings. The successful application of US in producing a uniform microstructure throughout the castings, suggests that a master alloy with, for e.g., 10 wt % nanoparticles, manufactured by this method, may feasibly be added to the base alloy when conventionally cast. Also, the results of the recycled castings make it feasible to use the initial nanocomposite materials as feedstock for casting processes where the additional cost of adding an ultrasonic system is cost prohibitive.

4.3. Comparison of Yield Strength Prediction by Models

Various models describe the increase in yield strength in nanocomposites, whereby the mechanisms for increasing the strength are based on the following microstructural effects: Orowan strengthening, grain refinement, dislocation generation due to differences in the coefficient of thermal expansion (CTE) or modulus, and the load-bearing mechanism. Kim et al. described the prediction of strengthening effects in MMNCs based on magnesium [20]. Arithmetic summation of the strengthening contributions can result in an overestimation in some cases [38,39]. This method is one of two methods used in this study because the strengthening mechanisms are considered to be independent of each other. The other method used is quadratic summation that is based on larger, micron-sized particles and assumes interaction between the individual strengthening mechanisms, which is more likely to be the case when larger particles act as reinforcement.

Under the precondition that the addition of nanoparticles reduces the grain size compared to the unreinforced alloy cast under exactly the same conditions, the improvement in yield strength can be described by Equation (A2) in Appendix A.

As mentioned above, the term in brackets is called grain size reduction, where D_{MMNC} and D_0 , the grain size in the nanocomposite and the unreinforced alloy, respectively, are processed in the same way. Values for GSR are $8.05 \times 10^{-2} \mu\text{m}^{-1/2}$ for the as-cast nanocomposite and $6.58 \times 10^{-2} \mu\text{m}^{-1/2}$, $4.72 \times 10^{-2} \mu\text{m}^{-1/2}$, and $4.34 \times 10^{-2} \mu\text{m}^{-1/2}$ for castings of the first, second, and third remelting, respectively.

Taking the grain sizes from Table 1 and k_y to be $530.2 \text{ MPa } \mu\text{m}^{1/2}$, the strengthening contribution from grain size reduction according to Equation (A2) is 42.7 MPa for the as-cast nanocomposite, and 34.9 MPa, 25.0 MPa, and 23.0 MPa for the first, second, and third remelted nanocomposites. The strength increase due to grain refinement after Equation (A2) for the recycled materials is close to the measured strength increase. There is a gap of 3.6 MPa for the as-cast AM60 + AlN that may be generated by one of the other strengthening mechanisms mentioned above.

It may be assumed that Orowan strengthening contributes to the total increase in strength as well. Zhang and Chen proposed a description for the Orowan contribution $\Delta\sigma_{\text{OR}}$ to strengthening [40] given by Equation (A3) in Appendix A.

V_p is the volume fraction of 1 wt % AlN nanoparticles ($\approx 5.5214 \times 10^{-3}$), G_m is the shear modulus of the matrix alloy (16.6 GPa), d_p is the average diameter of the AlN nanoparticles (80 nm), and b the Burgers vector of the matrix (0.32 nm). Applying these structural parameters, the Orowan contribution to strengthening is calculated to be 11.9 MPa, which is larger than the gap between the measured yield strength and the contribution of Hall-Petch strengthening, when applying arithmetic summation.

Geometrically necessary dislocations (GND) contribute to strengthening too. These dislocations are created during cooling due to mismatch in the Coefficient of Thermal Expansion (CTE) between the matrix and that of the reinforcement. The strengthening contribution of CTE mismatch during cooling down from the casting temperature to room temperature can be calculated according to Equation (A5) in Appendix A [39,41], where β is considered to be 1.25 [41], $\Delta\alpha$ is the difference between the CTE of the matrix ($28.5 \times 10^{-6} \text{ K}^{-1}$), and AlN-particles ($4.5 \times 10^{-6} \text{ K}^{-1}$), and ΔT is the difference between the processing temperature and tensile test temperature (room temperature). It needs to be mentioned that particles smaller than a critical diameter d^* are not expected to contribute to CTE-strengthening. In an Al/Al₂O₃ system, Redsten et al. [42,43] proposed Equation (A6) in Appendix A for calculating the critical size. Although solidification is finished at 543 °C, all generated mismatch created at

high temperatures down to a homologous temperature of 0.59 (~210 °C) or only 0.55 (176 °C) [43] is expected to relax by diffusion, so that ΔT is only 190 °C or 155 °C. Taking the mean value 172.5 °C for ΔT , the critical diameter d^* is calculated to be 87.4 nm. Having a medium particle size of 80 nm, the influence of CTE mismatch on strengthening of the material is assumed to be negligible.

Other strengthening mechanisms like modulus mismatch strengthening, which creates GND due to differences in elastic moduli of reinforcement and matrix alloy when subjected to compressive stresses, can be neglected in this case. It needs to be taken into account only when materials are post-processed, for e.g., in wrought processes, like extrusion, forging, or rolling, where compressive stresses are applied.

Load bearing strengthening can be neglected in MMNCs with low volume fraction of nanoparticles, as well. Following Equation (A7) in Appendix A [20], the strengthening contribution of the load bearing effect $\Delta\sigma_{\text{Load}}$ in the investigated system is 0.12 MPa, assuming a well bonded spherical particle in the matrix.

The above calculations show that the main strengthening contribution of 42.7 MPa comes from grain size reduction as a consequence of nanoparticle addition. Orowan strengthening contributed 11.9 MPa to yield strength improvement. Other effects can be ignored due to only small contributions to strength. Neither GND dislocations due to CTE mismatch or modulus mismatch nor the load bearing effect significantly improves yield strength. As mentioned above, either arithmetic (Equation (A8) in Appendix A) or quadratic (Equation (A9) in Appendix A) summation can be applied.

Following Equation (A8) a total strength increase of 54.8 MPa can be assumed. Experimentally we found an increase of 46.3 MPa. The arithmetic summation method, therefore, results in an overestimation of yield strength increase, but is acceptable. The quadratic summation method of Equation (A9) results in an increase of 44.3 MPa, which is slightly below the experimental yield strength increase. Thus, both methods result in acceptable estimations.

5. Conclusions

An AM60 based nanocomposite containing 1 wt % of AlN particles with an average size of 80 nm was successfully produced using an ultrasound assisted indirect chill casting process. Castings were remelted three times in order to evaluate the microstructure and mechanical properties of each cast nanocomposite. The as-cast nanocomposite is significantly grain refined compared to the AlN-free AM60 processed in the same way including stirring and ultrasonic treatment. A nucleation-free zone (NFZ) formed around each grain prevents further nucleation and, thus, limits the grain size to approximately that of the size of NFZ. The addition of AlN nanoparticles under ultrasound treatment produced remarkable improvements in mechanical properties: yield strength increased by 103%, ultimate tensile strength by 115%, and ductility by 140%. By modelling the possible strengthening mechanisms, the main contribution to yield strength is provided by Hall-Petch strengthening and a small amount from Orowan strengthening. There is a negligible contribution from the CTE mismatch mechanism. Whereas the arithmetic summation of strengthening effects overestimates the yield strength increase, the quadratic summation method slightly underestimates it. After each remelting of the as-cast nanocomposite, the yield strength, ultimate tensile strength, and ductility slightly decreased while the grain size increased. These effects are interrelated according to Hall-Petch strengthening. The small change in mechanical properties after remelting suggests the ultrasonically processed nanocomposite is suitable for use and re-use in a range of casting processes.

Acknowledgments: The authors wish to acknowledge financial support from the European Commission (ExoMet Project, 7th Framework Programme, contract FP7-NMP3-LA-2012-280421). David StJohn acknowledges the support of the Australian Research Council Discovery Grant DP140100702. Sergey Vorozhtsov acknowledges the support of Russian Science Foundation Grant (project No. 17-13-01252). The authors thank Hamdi Tek for performing the tensile tests and Günter Meister for casting.

Author Contributions: Hajo Dieringa contributed the casting of materials, strengthening calculations, idea of the paper, and coordination of authors; Lydia Katsarou, Ricardo Buzolin, and Gábor Szakács contributed metallography, grain size measurement, and hardness testing; Manfred Horstmann contributed the evaluation of

tensile tests; Martin Wolff contributed the DSC tests; Chamini Mendis contributed mismatch calculations based on the crystal structure; Sergey Vorozhtsov contributed the AlN nanoparticles and their properties; and David StJohn contributed the grain refinement calculation.

Conflicts of Interest: The authors declare no conflict of interest.

Appendix A

Hall-Petch relation: (Equation (A1)), where σ_y is the yield stress, σ_0 is the friction stress that allows dislocations to move on slip planes in a single crystal in the absence of any strengthening mechanisms, k_y is the stress concentration factor, and D is the average grain size [44,45].

$$\sigma_y = \sigma_0 + k_y D^{-1/2} \quad (\text{A1})$$

The improvement in yield strength can also be described with Equation (A2) if grain refinement by addition of nanoparticles cast under exactly the same conditions is assumed [20], where D_{MMNC} and D_0 are the grain size in the nanocomposite and the unreinforced alloy, respectively:

$$\Delta\sigma_{\text{GR}} = k_y \left(\frac{1}{\sqrt{D_{\text{MMNC}}}} - \frac{1}{\sqrt{D_0}} \right) \quad (\text{A2})$$

Orowan strengthening: Zhang and Chen proposed a description for the Orowan contribution $\Delta\sigma_{\text{OR}}$ to strengthening [40] given by the following equation, Equation (A3):

$$\Delta\sigma_{\text{OR}} = \frac{0.13bG_m}{\lambda} \ln \frac{d_p}{2b} \quad (\text{A3})$$

$$\text{where } \lambda = d_p \left[\left(\frac{1}{2V_p} \right)^{1/3} - 1 \right] \quad (\text{A4})$$

CTE mismatch: The strengthening contribution of CTE mismatch during cooling down from the casting temperature to room temperature can be calculated according to Equation (A5) [39,41].

$$\Delta\sigma_{\text{CTE}} = \sqrt{3}\beta G_m b \sqrt{\frac{12V_p \Delta\alpha \Delta T}{bd_p}} \quad (\text{A5})$$

Particles smaller than a critical diameter d^* are not expected to contribute to CTE-strengthening. In an Al/Al₂O₃ system, Redsten et al. [42,43] proposed Equation (A6) for calculating the critical size:

$$d^* = \frac{b}{\Delta\alpha \Delta T} \quad (\text{A6})$$

Load bearing strengthening:

$$\Delta\sigma_{\text{Load}} = \frac{1}{2} V_p \sigma_m \quad (\text{A7})$$

Arithmetic (Equation (A8)) or quadratic (Equation (A9)) summation of contributions to yield strength increase:

$$\Delta\sigma_{\text{Total}} = \Delta\sigma_{\text{GR}} + \Delta\sigma_{\text{OR}} + \Delta\sigma_{\text{CTE}} + \Delta\sigma_{\text{Mod}} + \Delta\sigma_{\text{Load}} \quad (\text{A8})$$

$$\Delta\sigma_{\text{Total}} = \sqrt{\Delta\sigma_{\text{GR}}^2 + \Delta\sigma_{\text{OR}}^2 + \Delta\sigma_{\text{CTE}}^2 + \Delta\sigma_{\text{Mod}}^2 + \Delta\sigma_{\text{Load}}^2} \quad (\text{A9})$$

References and Note

1. Gavras, S.; Zhu, S.M.; Nie, J.F.; Gibson, M.A.; Easton, M.A. On the microstructural factors affecting creep resistance of die-cast Mg-La-rare earth (Nd, Y or Gd) alloys. *Mater. Sci. Eng.* **2016**, *675*, 65–75. [[CrossRef](#)]

2. Zhu, S.M.; Gibson, M.A.; Easton, M.A.; Nie, J.F. The relationship between microstructure and creep resistance in die-cast magnesium-rare earth alloys. *Scr. Mater.* **2010**, *63*, 698–703. [[CrossRef](#)]
3. Moreno, I.P.; Nandy, T.K.; Jones, J.W.; Allison, J.E.; Pollock, T.M. Microstructural stability and creep of rare-earth containing magnesium alloys. *Scr. Mater.* **2003**, *48*, 1029–1034. [[CrossRef](#)]
4. Deming, H.; Yungui, C.; Yongbai, T.; Hongmei, L.; Gao, N. Indentation creep behavior of AE42 and Ca-containing AE41 alloys. *Mater. Lett.* **2007**, *61*, 1015–1019. [[CrossRef](#)]
5. Wan, X.; Sun, Y.; Xue, F. Microstructure and mechanical properties of ZA62 based magnesium alloys with calcium addition. *Trans. Nonferr. Met. Soc. China* **2010**, *20*, 757–762. [[CrossRef](#)]
6. Dargusch, M.S.; Zhu, S.M.; Nie, J.F.; Dunlop, G.L. Microstructural analysis of the improved creep resistance of a die-cast magnesium-aluminium-rare earth alloy by strontium additions. *Scr. Mater.* **2009**, *60*, 116–119. [[CrossRef](#)]
7. Zhao, P.; Wang, Q.; Zhai, C.; Zhu, Y. Effects of strontium and titanium on the microstructure, tensile properties and creep behavior of AM50 alloys. *Mater. Sci. Eng.* **2007**, *444*, 318–326. [[CrossRef](#)]
8. Mahmudi, R.; Moeendarbari, S. Effects of Sn additions on the microstructure and impression creep behaviour of AZ91magnesium alloy. *Mater. Sci. Eng.* **2013**, *566*, 30–39. [[CrossRef](#)]
9. Huang, Y.; Dieringa, H.; Kainer, K.U.; Hort, N. Understanding effects of microstructural inhomogeneity on creep response—New approaches to improve the creep resistance in magnesium alloys. *J. Magnes. Alloys* **2014**, *2*, 124–132. [[CrossRef](#)]
10. Dieringa, H.; Huang, Y.; Wittke, P.; Klein, M.; Walther, F.; Dikovits, M.; Poletti, C. Compression creep response of magnesium alloy DieMag422 containing barium compared with the commercial creep-resistant alloys AE42 and MRI230D. *Mater. Sci. Eng.* **2013**, *585*, 430–438. [[CrossRef](#)]
11. Trojanova, Z.; Szaraz, Z.; Labar, J.; Lukac, P. Deformation behaviour of an AS21 alloy reinforced by short Saffil fibres and SiC particles. *J. Mater. Proc. Technol.* **2005**, *162–163*, 131–138. [[CrossRef](#)]
12. Zhang, X.; Fang, L.; Xiong, B.; Hu, H. Microstructure and Tensile Properties of Mg (AM60)/Al₂O₃ Metal Matrix Composites with Varying Volume Fractions of Fiber Reinforcement. *J. Mater. Eng. Perform.* **2015**, *24*, 4601–4611. [[CrossRef](#)]
13. Mondal, A.K.; Kumar, S. Dry sliding wear behaviour of magnesium alloy based hybrid composites in the longitudinal direction. *Wear* **2009**, *267*, 458–466. [[CrossRef](#)]
14. Sklenicka, V.; Pahutova, M.; Kucharova, K.; Svoboda, M.; Langdon, T.G. Creep Processes in Magnesium Alloys and their Composites. *Metall. Mater. Trans.* **2002**, *33*, 883–889. [[CrossRef](#)]
15. Sklenicka, V.; Svoboda, M.; Pahutova, M.; Kucharova, K.; Langdon, T.G. Microstructural processes in creep of an AZ 91 magnesium-based composite and its matrix alloy. *Mater. Sci. Eng.* **2001**, *319–321*, 741–745. [[CrossRef](#)]
16. Viswanath, A.; Dieringa, H.; Ajith Kumar, K.K.; Pillai, U.T.S.; Pai, B.C. Investigation on mechanical properties and creep behavior of stir cast AZ91-SiCp composites. *J. Magnes. Alloys* **2015**, *3*, 16–22. [[CrossRef](#)]
17. Ochi, Y.; Masaki, K.; Matsumura, T.; Wadasako, M. Effects of volume fraction of alumina short fibers on high cycle fatigue properties of Al and Mg alloy composites. *Mater. Sci. Eng.* **2007**, *468–470*, 230–236. [[CrossRef](#)]
18. Huang, Y.D.; Hort, N.; Dieringa, H.; Maier, P.; Kainer, K.U. Investigations on thermal fatigue of aluminum- and magnesium-alloy based composites. *Int. J. Fatigue* **2006**, *28*, 1399–1405. [[CrossRef](#)]
19. Fu, H.M.; Zhang, M.-X.; Qiu, D.; Kelly, P.M.; Taylor, J.A. Grain refinement by AlN particles in Mg-Al based alloys. *J. Alloys Compd.* **2009**, *478*, 809–812. [[CrossRef](#)]
20. Kim, C.-S.; Sohn, I.; Nezafati, M.; Ferguson, J.B.; Schultz, B.F.; Bajestani-Gohari, Z.; Rohatgi, P.K.; Cho, K. Prediction models for the yield strength of particle-reinforced unimodal pure magnesium (Mg) metal matrix nanocomposites (MMNCs). *J. Mater. Sci.* **2013**, *48*, 4191–4204. [[CrossRef](#)]
21. Paramsothy, M.; Gupta, M. The opposing nanoscale and macroscale effects of selected nanoparticle addition to AZ91/ZK60A hybrid magnesium alloy. *J. Nanopart. Res.* **2013**, *15*, 1938–1950. [[CrossRef](#)]
22. Paramsothy, M.; Chan, J.; Kwok, R.; Gupta, M. Nitride nanoparticle addition to beneficially reinforce hybrid magnesium alloys. *Metall. Mater. Trans.* **2013**, *44*, 1123–1138. [[CrossRef](#)]
23. Dieringa, H. Properties of magnesium alloys reinforced with nanoparticles and carbon nanotubes: A review. *J. Mater. Sci.* **2011**, *46*, 289–306. [[CrossRef](#)]
24. Tan, X.; How, W.C.K.; Weng, J.C.K.; Onn, R.K.W.; Gupta, M. Development of high-performance quaternary LPSO Mg-Y-Zn-Al alloys by Disintegrated Melt Deposition technique. *Mater. Des.* **2015**, *83*, 443–450.

25. Hassan, S.; Gupta, M. Development of a novel magnesium-copper based composite with improved mechanical properties. *Mater. Res. Bull.* **2002**, *37*, 377–389. [[CrossRef](#)]
26. Chen, L.-Y.; Xu, J.; Choi, H.; Pozuelo, M.; Ma, X.; Bhowmick, S.; Yang, J.; Mathaudhu, S.; Li, X. Processing and properties of magnesium containing a dense uniform dispersion of nanoparticles. *Nature* **2015**, *528*, 539–543. [[CrossRef](#)] [[PubMed](#)]
27. Sillekens, W.H.; Jarvis, D.J.; Vorozhtsov, A.; Bojarevics, V.; Badini, C.F.; Pavese, M.; Terzi, S.; Salvo, L.; Katsarou, L.; Dieringa, H. The ExoMet Project: EU/ESA Research on High-Performance Light-Metal Alloys and Nanocomposites. *Metall. Mater. Trans.* **2014**, *45*, 3349–3361. [[CrossRef](#)]
28. Katsarou, L.; Mounib, M.; Lefebvre, W.; Vorozhtsov, S.; Pavese, M.; Badini, C.; Molina-Aldareguia, J.M.; Cepeda Jimenez, C.; Pérez Prado, M.T.; Dieringa, H. Microstructure, mechanical properties and creep of magnesium alloy Elektron21 reinforced with AlN nanoparticles by ultrasound-assisted stirring. *Mater. Sci. Eng.* **2016**, *659*, 84–92. [[CrossRef](#)]
29. Lerner, M.; Vorozhtsov, A.; Guseinov, S.; Storozhenko, P. Metal Nanopowders Production. In *Metal Nanopowders: Production, Characterization, and Energetic Applications*; Gromov, A.A., Teipel, U., Eds.; Wiley-VCH: Hoboken, NJ, USA, 2014; pp. 79–106, ISBN 9783527680726.
30. Pearson's—Crystal Structure Database for Inorganic Compounds (on CD-ROM); Villars, P., Cenzual, K., Eds.; Release 2015/16.
31. Somekawa, H.; Mukai, T. Effect of grain refinement on fracture toughness in extruded pure magnesium. *Scr. Mater.* **2005**, *53*, 1059–1064. [[CrossRef](#)]
32. Kang, S.H.; Lee, Y.S.; Lee, J.H. Effect of grain refinement of magnesium alloy AZ31 by severe plastic deformation on material characteristics. *J. Mater. Proc. Technol.* **2008**, *201*, 436–440. [[CrossRef](#)]
33. Mukai, T.; Yamanoi, M.; Watanabe, H.; Ishikawa, K.; Higashi, K. Effect of grain refinement on tensile ductility in ZK60 magnesium alloy under dynamic loading. *Mater. Trans.* **2001**, *42*, 1177–1181. [[CrossRef](#)]
34. StJohn, D.H.; Prasad, A.; Easton, M.A.; Qian, M. The contribution of constitutional supercooling to nucleation and grain formation. *Metall. Mater. Trans.* **2015**, *46*, 4868–4885. [[CrossRef](#)]
35. Greer, A.L.; Bunn, A.M.; Tronche, A.; Evans, P.V.; Bristow, D.J. Modelling of inoculation of metallic melts: Application to grain refinement of aluminium by AlTiB. *Acta Mater.* **2000**, *48*, 2823–2835. [[CrossRef](#)]
36. StJohn, D.H.; Qian, M.; Easton, M.A.; Cao, P. The Interdependence Theory: The relationship between grain formation and grain selection. *Acta Mater.* **2011**, *59*, 4907–4921. [[CrossRef](#)]
37. Poirier, D.R. Density, viscosity, and diffusion coefficients in hypoeutectic Al-Si liquid alloys: An assessment of available data. *Metall. Mater. Trans.* **2014**, *45*, 1345–1354. [[CrossRef](#)]
38. Goh, C.S.; Wei, J.; Lee, L.C.; Gupta, M. Properties and deformation behaviour of Mg-Y₂O₃ nanocomposites. *Acta Mater.* **2007**, *55*, 5115–5121. [[CrossRef](#)]
39. Dai, L.H.; Ling, Z.; Bai, Y.L. Size-dependent inelastic behavior of particle-reinforced metal-matrix composites. *Compos. Sci. Technol.* **2001**, *61*, 1057–1063. [[CrossRef](#)]
40. Zhang, Z.; Chen, D.L. Consideration of Orowan strengthening effect in particulate-reinforced metal matrix nanocomposites: A model for predicting their yield strength. *Scr. Mater.* **2006**, *54*, 1321–1326. [[CrossRef](#)]
41. Vogt, R.; Zhang, Z.; Li, Y.; Bonds, M.; Browning, N.D.; Lavernia, E.J.; Schoenung, J.M. The absence of thermal expansion mismatch strengthening in nanostructured metal-matrix composites. *Scr. Mater.* **2009**, *61*, 1052–1055. [[CrossRef](#)]
42. Redsten, A.M.; Klier, E.M.; Brown, A.M.; Dunand, D.C. Mechanical properties and microstructure of cast oxide-dispersion-strengthened aluminium. *Mater. Sci. Eng.* **1995**, *201*, 88–102. [[CrossRef](#)]
43. Dunand, D.C.; Mortensen, A. On plastic relaxation of thermal stresses in reinforced metals. *Acta Metall. Mater.* **1991**, *39*, 127–139. [[CrossRef](#)]
44. Hall, E.O. The deformation and Ageing of mild steel: III Discussion of Results. *Phys. Soc.* **1951**, *64*, 747–753. [[CrossRef](#)]
45. Petch, N.J. The Cleavage Strength of Polycrystals. *J. Iron Steel Inst.* **1953**, *174*, 25–28.

